Received May 16, 2020, accepted May 31, 2020, date of publication June 3, 2020, date of current version June 15, 2020.

Digital Object Identifier 10.1109/ACCESS.2020.2999647

Vector Control of Asymmetric Dual Three-Phase PMSM in Full Modulation Range

YUAN ZHU[1,2], WEISONG GU[1], KE LU[1,2], AND ZHIHONG WU[1,2], (Member, IEEE)

[1]School of Automotive Studies, Tongji University, Shanghai 201800, China
[2]Sino-German School for Post-Graduate Studies, Tongji University, Shanghai 201800, China

Corresponding author: Ke Lu (luke@tongji.edu.cn)

This work was supported by the National Key Research and Development Program of China under Grant 2016YFB0100804.

ABSTRACT The total control range of asymmetric dual three-phase permanent magnet synchronous motor (ADT_PMSM) is divided into three different segments by voltage modulation range and current control dimensions and respective control strategies to get the injected voltages in harmonic subspace for three segments are presented in this paper. The three segments are sinusoidal current modulation region, sinusoidal voltage modulation region and overmodulation region. In sinusoidal current modulation region, resonant controller is adopted in the harmonic subspace to calculate the injected voltages, which can compensate the effect of six-phase voltage source inverter (VSI) dead time for two sets of three-phase windings and takes the pole correction into consideration. In sinusoidal voltage modulation region, open loop control strategy in harmonic subspace is adopted. Overmodulation region 1 and 2 are defined in overmodulation region, and the harmonic voltages which are injected into harmonic subspace to extend the modulation index are calculated based on superposition principle and VSD theory. In order to achieve smooth transition from different regions, a novel space vector pulse width modulation (SVPWM) technique for ADT_PMSM is proposed. The experimental results demonstrate the validity and feasibility of the suggested control approach.

INDEX TERMS Asymmetric dual three-phase permanent magnet synchronous motor, modulation index, dimensions of current control, modulation region, space vector pulse width modulation.

I. INTRODUCTION

Multi-phase motors received considerable attention lately thanks to the unique characteristics of higher fault tolerance, smaller torque ripples, advanced control strategies and the rapid development of the multilevel inverters [1]–[6]. Among these multiphase motors, ADT_PMSM can have the advantages of multi-phase machines [3]. They also make full use of the modular structure of conventional three-phase machines as shown in Fig.1, which consists of two identical sets of three-phase windings shifted by 30 degrees with isolated neutral points.

The vector space decomposition (VSD) is widely employed for the vector control of ADT_PMSM because it can take the advantages of multi-degree freedom of multi-phase motors, which includes two kinds of current control as follows.

1) Two-dimension current control [7]–[10] can only control the currents in α-ß subspace where the variables in this subspace participate in electromechanical energy conversion. While the reference voltages in x-y subspace is controlled to zero by the appropriate pulse width modulation (PWM) algorithm [7] or optimized switching-table-based direct torque control (ST_DTC) strategies [8]–[10]. But the 5th and 7th current harmonics because of the nonlinearities of inverter are mapped into x-y subspace, which will produce larger harmonic currents. Therefore, two-dimension current control cannot achieve desired performances in practical applications.

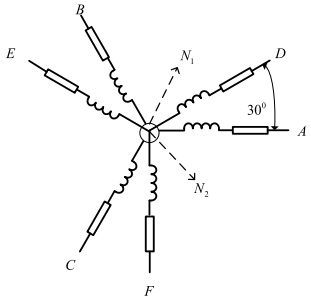

FIGURE 1. Phase winding diagram of ADT_PMSM.

The associate editor coordinating the review of this manuscript and approving it for publication was Fabio Massaro.

2) Four-dimension current control can establish closed loop control strategies in two subspaces simultaneously. The harmonic currents in *x-y* subspace are suppressed to zero by closed-loop controller in this subspace, which shows better performances in harmonic current suppression [11]–[18].

Because of the advantages of four-dimension current control on the basis of the VSD theory, a lot research findings set up closed current loop control in both subspaces in the linear modulation region, which can make compensations for dead time caused by the nonlinear characteristics of inverter. PI controllers of parallel connection based on multiple synchronous frames (MSF) scheme (one per harmonic) are adopted in the harmonic subspace to suppress the harmonic currents in multiphase motors, and zero steady-state error can be achieved at different orders [11]. But it adds complexity to the computation. Resonant controller can be a perfect substitute for PI regulators based on MSF in parallel connection [12]–[15]. The calculation complexity is reduced in comparison with the implementation of PI controller in MSF in parallel [14], [15]. Accordingly, an improved resonant controller in [16]–[18] on the basis of a novel synchronous rotating matrix is employed in *x-y* subspace to eliminate the harmonic currents. However, the results are not as expected because they don't take the pole errors at the resonant frequency into account.

Extra voltages should be injected into the harmonic subspace so that the ADT_PMSM can operate in the overmodulation region, so the currents cannot be controlled in the harmonic subspace in the overmodulation region. Two-vector space vector pulse width modulation (SVPWM) technique can easily be extended to the overmodulation region. But it injects large amount of harmonic voltages into the harmonic subspace, which will lead to heavy harmonic currents [19], [20]. Accordingly, four-vector SVPWM is employed to reduce the injected harmonic voltage into harmonic subspace [21], [22]. However, it cannot achieve the minimum injected harmonic voltages. In [23], minimum injected harmonic voltages into *x-y* subspace can be achieved. But the modulation index can only reach 0.9883. Besides, the PWM waveforms of the methods mentioned above are not symmetric on condition that the switching device is guaranteed to turn-on and-off only once in each PWM period [19]. In [7], a simple classification algorithm is utilized and the three-phase SVPWM algorithm is employed to achieve PWM implementation. It can achieve the maximum modulation index, which is proved to be equal to the maximum modulation index of three-phase motors [24], [25], but large current harmonics arise because of the injected voltage harmonics and small leakage inductance in harmonic subspace. For the sake of minimizing the current harmonics in *x-y* subspace, optimal PWM algorithm is adopted, which can synthesize the voltage vectors in both subspaces at the same time. However, the complexity to solve the optimization problem is very heavy. Two methods of optimization are adopted for the five-phase motors [26], [27], takes the common mode voltage into account.

TABLE 1. Comparison with other literature findings.

References	Linear modulation	Overmodulation
7-18	√	
19-27		√

Besides, none of the research findings give the division principle between the linear modulation region and the overmodulation region to the knowledge of authors. This paper gives the division principle for the full modulation range and respective control strategies in the different modulations. And other research findings cannot cover the whole modulation range. References [7]–[13] only studied the linear modulation region, while [19]–[28] only discuss the overmodulation region as shown in Table 1. Besides, the performances in each modulation region are not as expected.

This paper is structured in the following way. Section 2 gives PWM techniques and divisions of modulation regions for ADT_PMSM in full modulation range. The control methods for the linear modulation region and overmodulation region are presented in section 3 and section 4 respectively. Section 5 gives the experimental results. Section 6 concludes this paper.

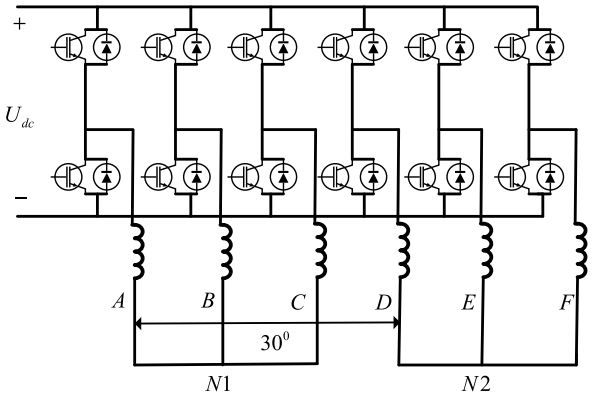

FIGURE 2. Phase windings of ADT_PMSM fed by two three-phase VSIs.

II. PWM TECHNIQUES AND DIVISIONS OF MODULATION REGION FOR ADT_PMSM IN FULL MODULATION RANGE

Fig.2 gives the structure of ADT-PMSM. It consists of two sets of three-phase windings, which are identical and supplied by two three-phase VSIs.

Based on the VSD theory [18], the motor variables (including flux, voltage and current) are mapped into three subspaces which are orthogonal to each other, i.e., α-β (fundamental), *x-y* (harmonic) and O_1-O_2 subspaces. The fundamental component and the 12n±1 order harmonic components make contributions to the electromechanical energy conversion and are mapped into α-β subspace. The *x-y* subspace contains harmonics of the orders 6n±1, which only give rises to losses and should be eliminated to get a higher efficiency of ADT_PMSM. The zero sequence component and harmonic orders of 3n exist in O_1-O_2 subspace, which are not taken into

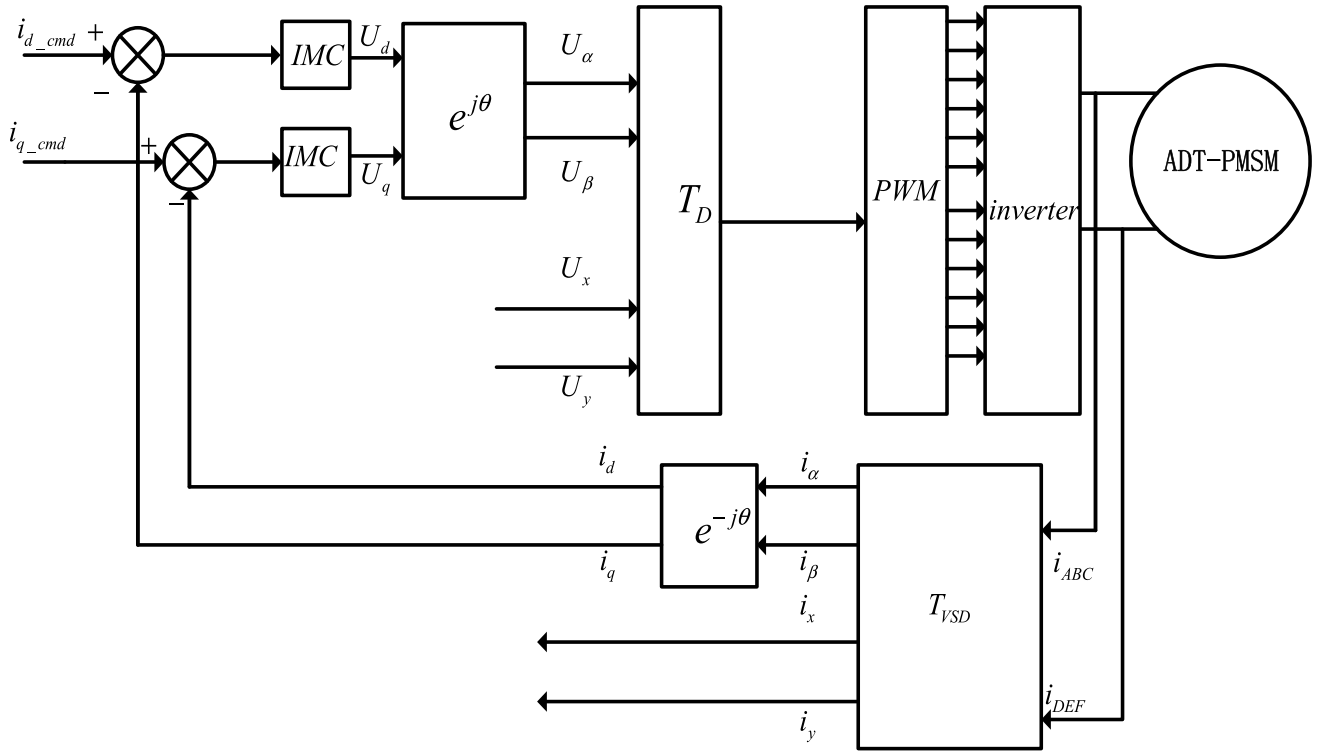

FIGURE 3. Current control block diagram for ADT_PMSM.

consideration since the neutral points are isolated and they cannot flow. Therefore, the control system for ADT_PMSM on the basis of VSD theory can be viewed as a four-order system and it needs current controller in both α-β and x-y subspaces. The relation between the double dq modelling scheme and VSD modelling approach is discussed in [18]. The VSD transformation based on the magnitude invariant principle can be obtained in equation (1).

$$T_{VSD} = \frac{1}{3}\begin{bmatrix} 1 & -\frac{1}{2} & -\frac{1}{2} & \frac{\sqrt{3}}{2} & -\frac{\sqrt{3}}{2} & 0 \\ 0 & \frac{\sqrt{3}}{2} & -\frac{\sqrt{3}}{2} & \frac{1}{2} & \frac{1}{2} & -1 \\ 1 & -\frac{1}{2} & -\frac{1}{2} & -\frac{\sqrt{3}}{2} & \frac{\sqrt{3}}{2} & 0 \\ 0 & -\frac{\sqrt{3}}{2} & \frac{\sqrt{3}}{2} & \frac{1}{2} & \frac{1}{2} & -1 \end{bmatrix} \tag{1}$$

The phase currents of ADT_PMSM after the VSD matrix will be mapped into α-β and x-y subspaces, which can be expressed in equation (2). The other variables (flux, voltage) can be derived in a similar way.

$$\begin{bmatrix} i_\alpha & i_\beta & i_x & i_y \end{bmatrix}^T = T_{VSD} * \begin{bmatrix} i_A & i_B & i_C & i_D & i_E & i_F \end{bmatrix}^T \tag{2}$$

Fig. 3 depicts the current control block diagram of ADT_PMSM on the basis of VSD theory. In α-β subspace, U_α and $U_ß$ can be acquired by the internal model control (IMC) method which can be found in [16], [17]. In x-y subspace, U_x and U_y can be determined according to the modulation region, which will be discussed in the following sections.

U_x and U_y can be determined in terms of the control strategies in different modulation regions, which will be discussed in the following sections. The reference voltage vectors in α-β and x-y subspaces are given in vector form as in equation (3).

$$\overrightarrow{U_{\alpha\beta}} = U_\alpha + jU_\beta \overrightarrow{U_{xy}} = U_x + jU_y \tag{3}$$

The reference voltage vectors in both α-β and x-y subspaces are supposed to be modulated by the six-phase VSI simultaneously. And they could be resolved into two groups of voltage vectors for two three-phase VSIs shifted by 30 electrical degrees through the matrix T_D as in equation (4).

$$T_D = \begin{bmatrix} 1 & 0 & 1 & 0 \\ 0 & 1 & 0 & -1 \\ \frac{\sqrt{3}}{2} & \frac{1}{2} & -\frac{\sqrt{3}}{2} & \frac{1}{2} \\ -\frac{1}{2} & \frac{\sqrt{3}}{2} & \frac{1}{2} & \frac{\sqrt{3}}{2} \end{bmatrix} \tag{4}$$

After employing the matrix T_D, the voltage vectors for two three-phase VSIs shifted by 30 electrical degrees can be given in equation (5).

$$\begin{bmatrix} U_{\alpha 1} & U_{\beta 1} & U_{\alpha 2} & U_{\beta 2} \end{bmatrix}^T = T_D * \begin{bmatrix} U_\alpha & U_\beta & U_x & U_y \end{bmatrix}^T \tag{5}$$

The modulation section can be divided into 12 sectors as depicted in Fig. 4.

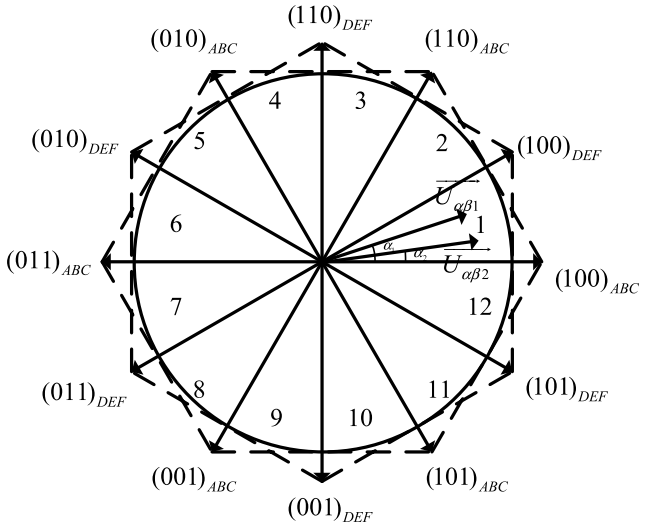

FIGURE 4. The division of modulation section for ADT_PMSM.

Assuming that the reference voltage vector resides in sector 1. The traditional SVPWM technique for three-phase motors can be adopted, which can achieve the maximum fundamental component $2U_{dc}/\pi$. Switching vectors (100) and (110) are adopted for windings ABC, while the windings DEF chooses the switching vectors (100) and (101). The following equations can be derived in terms of the volt-second balance principle.

$$\begin{cases} \overrightarrow{U_{\alpha\beta1}}T_s = \overrightarrow{U_{100ABC}}T_{100ABC} + \overrightarrow{U_{110ABC}}T_{110ABC} \\ \overrightarrow{U_{\alpha\beta2}}T_s = \overrightarrow{U_{100DEF}}T_{100DEF} + \overrightarrow{U_{101DEF}}T_{101DEF} \\ \overrightarrow{U_{\alpha\beta1}} = U_{\alpha1} + jU_{\beta1} \\ \overrightarrow{U_{\alpha\beta2}} = U_{\alpha2} + jU_{\beta2} \end{cases} \tag{6}$$

So the on-durations for the switching vectors of two three-phase windings can be given by

$$\begin{cases} T_{100ABC} = \dfrac{\sqrt{3}\left|\overrightarrow{U_{\alpha\beta1}}\right|}{U_{dc}} T_s \sin(\dfrac{\pi}{3} - \alpha_1) \\ T_{110ABC} = \dfrac{\sqrt{3}\left|\overrightarrow{U_{\alpha\beta1}}\right|}{U_{dc}} T_s \sin\alpha_1 \\ T_{100DEF} = \dfrac{\sqrt{3}\left|\overrightarrow{U_{\alpha\beta2}}\right|}{U_{dc}} T_s \sin\left(\alpha_2 + \dfrac{\pi}{6}\right) \\ T_{101DEF} = \dfrac{\sqrt{3}\left|\overrightarrow{U_{\alpha\beta2}}\right|}{U_{dc}} T_s \sin\left[\dfrac{\pi}{3} - (\alpha_2 + \dfrac{\pi}{6})\right] \end{cases} \tag{7}$$

where α_1 and α_2 are the vector angles of $\overrightarrow{U_{\alpha\beta1}}$ and $\overrightarrow{U_{\alpha\beta2}}$ respectively as depicted in Fig.4, which can be expressed as

$$\begin{cases} \alpha_1 = \arctan\left|\dfrac{U_{\beta1}}{U_{\alpha1}}\right| \\ \alpha_2 = \arctan\left|\dfrac{U_{\beta2}}{U_{\alpha2}}\right| \end{cases} \tag{8}$$

The modulation index M for ADT_PMSM can inherit the modulation index for three-phase motors, which can be defined as

$$M = \frac{\pi}{2}\frac{\left|\overrightarrow{U_{\alpha\beta}}\right|}{U_{dc}} \tag{9}$$

where $\overrightarrow{U_{\alpha\beta}} = U_\alpha + jU_\beta$

Linear modulation region and overmodulation region can be defined according to the modulation index M. When $0 \leq M \leq 0.9069$, ADT_PMSM operates in linear modulation region. When $0.9069 < M \leq 1$, ADT_PMSM operates in overmodulation region.

According to the inverse transformation of VSD matrix, the phase voltages of ADT_PMSM can be expressed as

$$\begin{cases} U_A = \left|\overrightarrow{U_{\alpha\beta}}\right|\cos\gamma + \left|\overrightarrow{U_{xy}}\right|\cos\gamma_z \\ U_B = \left|\overrightarrow{U_{\alpha\beta}}\right|\cos(\gamma - \dfrac{2\pi}{3}) + \left|\overrightarrow{U_{xy}}\right|\cos(\gamma_z + \dfrac{2\pi}{3}) \\ U_C = \left|\overrightarrow{U_{\alpha\beta}}\right|\cos(\gamma + \dfrac{2\pi}{3}) + \left|\overrightarrow{U_{xy}}\right|\cos(\gamma_z - \dfrac{2\pi}{3}) \\ U_D = \left|\overrightarrow{U_{\alpha\beta}}\right|\cos(\gamma - \dfrac{\pi}{6}) + \left|\overrightarrow{U_{xy}}\right|\cos(\gamma_z - \dfrac{5\pi}{6}) \\ U_E = \left|\overrightarrow{U_{\alpha\beta}}\right|\cos(\gamma - \dfrac{5\pi}{6}) + \left|\overrightarrow{U_{xy}}\right|\cos(\gamma_z - \dfrac{\pi}{6}) \\ U_F = \left|\overrightarrow{U_{\alpha\beta}}\right|\cos(\gamma + \dfrac{\pi}{2}) + \left|\overrightarrow{U_{xy}}\right|\cos(\gamma_z + \dfrac{\pi}{2}) \end{cases} \tag{10}$$

where $\overrightarrow{U_{xy}} = U_x + jU_y$

The line voltage U_{AB} can be calculated in equation (11).

$$U_{AB} = -\sqrt{3}\left|\overrightarrow{U_{\alpha\beta}}\right|\sin(\gamma - \frac{\pi}{3}) + \sqrt{3}\left|\overrightarrow{U_{xy}}\right|\sin\left(\gamma_z + \frac{\pi}{3}\right) \tag{11}$$

The other line voltages can be expressed in the similar form as equation (11). The amplitude of line voltage must be smaller than the bus voltage.

$$|U_{AB}| \leq \sqrt{3}\left|\overrightarrow{U_{\alpha\beta}}\right| + \sqrt{3}\left|\overrightarrow{U_{xy}}\right| \leq U_{dc} \tag{12}$$

where U_{dc} denotes the bus voltage

Equation (12) can be simplified as follows.

$$\left|\overrightarrow{U_{\alpha\beta}}\right| + \left|\overrightarrow{U_{xy}}\right| \leq \frac{U_{dc}}{\sqrt{3}} \tag{13}$$

Therefore, the voltage vectors in both subspaces can be modulated on condition that the amplitudes of voltage vectors satisfy equation (13). And closed current control loops are designed in both subspaces, which can compensate for the dead time of inverter and can be called the sinusoidal current modulation area.

The maximal voltage vector that can be synthesized in α-β subspace is $U_{dc}/\sqrt{3}$ in the linear modulation region. So no current regulator is designed in x-y subspace when the voltage vector satisfies equation (14). The command voltage U_x and U_y are set to be zero without injecting extra harmonic voltages, which is two-dimension current control and can be called sinusoidal voltage modulation area.

$$\left|\overrightarrow{U_{\alpha\beta}}\right| + \left|\overrightarrow{U_{xy}}\right| > U_{dc}/\sqrt{3} \text{ and } \left|\overrightarrow{U_{\alpha\beta}}\right| \leq U_{dc}/\sqrt{3} \tag{14}$$

TABLE 2. The voltage modulation range of three vector control regions.

Modulation region	Vector control region	Voltage modulation range	Dimensions of current control
Linear modulation region 0≤M≤0.9069	Sinusoidal current region	$\lvert\overrightarrow{U_{\alpha\beta}}\rvert+\lvert\overrightarrow{U_{xy}}\rvert\le U_{dc}/\sqrt{3}$	Four dimensions
	Sinusoidal voltage region	$\lvert\overrightarrow{U_{\alpha\beta}}\rvert+\lvert\overrightarrow{U_{xy}}\rvert> U_{dc}/\sqrt{3}$ and $\lvert\overrightarrow{U_{\alpha\beta}}\rvert\le U_{dc}/\sqrt{3}$	Two dimensions
Overmodulation region (0.9069<M≤1)	Overmodulation region	$U_{dc}/\sqrt{3}<\lvert\overrightarrow{U_{\alpha\beta}}\rvert\le 2U_{dc}/\pi$	Two dimensions

When the voltage vector satisfies equation (15), injecting extra harmonic voltages into x-y subspace is necessary for the synthesis of voltage vector in α-β subspace, which can be called overmodulation area and contains a lot of harmonic currents.

$$U_{dc}/\sqrt{3} < \left|\overrightarrow{U_{\alpha\beta}}\right| \le 2U_{dc}/\pi \tag{15}$$

The voltage modulation range of three vector regions is illustrated in Table 2. It is remarked that equation (13) is a sufficient but not necessary condition that the voltage vectors can be synthesized at the same time, i.e., equation (13) corresponds to an arbitrary value of angle between $\overrightarrow{U_{\alpha\beta}}$ and $\overrightarrow{U_{xy}}$. The sum value of $\left|\overrightarrow{U_{\alpha\beta}}\right|$ and $\left|\overrightarrow{U_{xy}}\right|$ can still increase when the angle between $\overrightarrow{U_{\alpha\beta}}$ and $\overrightarrow{U_{xy}}$ satisfies a specific relationship. But the angle between $\left|\overrightarrow{U_{\alpha\beta}}\right|$ and $\left|\overrightarrow{U_{xy}}\right|$ can be any combination. It will be more complicated if all the cases are judged. So equation (13) is simple and effective though it is not absolutely correct to be used as the dividing principle for sinusoidal current modulation area and sinusoidal voltage modulation area.

III. CONTROL OF ADT_PMSM IN LINEAR MODULATION REGION

A. CURRENT HARMONIC ANALYSIS

After the VSD transformation [5], the current vector are expressed as follows.

$$\overrightarrow{i_{\alpha\beta}} = i_\alpha + ji_\beta = i_{\alpha1} + i_{\alpha2} + j(i_{\beta1} + i_{\beta2}) \tag{16}$$

$$\overrightarrow{i_{xy}} = i_x + ji_y = i_{\alpha1} - i_{\alpha2} - j(i_{\beta1} - i_{\beta2}) \tag{17}$$

The fifth and seventh current harmonics for two sets of three-phase windings can be given by

$$\begin{aligned}\overrightarrow{I}^{\,h}_{\alpha\beta1} &= k_1 Ie^{-5jw_et} + k_2 Ie^{7jw_et}\\ \overrightarrow{I}^{\,h}_{\alpha\beta2} &= k_3 Ie^{-5jw_et} + k_4 Ie^{7jw_et}\end{aligned} \tag{18}$$

And the weights of fifth and seventh current harmonics in phase windings ABC are represented by k_1 and k_2. k_3 and k_4 denote the weights of fifth and seventh harmonic currents of the other phase windings DEF.

Based on the equations (17),(18) and VSD theory, the current harmonics in x-y subspaces can be expressed in the following form.

$$\overrightarrow{I}^{\,h}_{xy} = (k_1 - k_3)Ie^{5jw_et} + (k_2 - k_4)Ie^{-7jw_et} \tag{19}$$

It is apparent that the fifth and seventh harmonic currents become +5th and -7th in x-y subspace. A novel synchronous rotating coordinate matrix is suggested here to transform the $+5w_e$ and $-7w_e$ current harmonics to $+6w_e$ and $-6w_e$ respectively as illustrated in equation (20).

$$T_T = \begin{bmatrix} \cos\theta & \sin\theta & 0 & 0 & 0 & 0 \\ -\sin\theta & \cos\theta & 0 & 0 & 0 & 0 \\ 0 & 0 & \cos\theta & -\sin\theta & 0 & 0 \\ 0 & 0 & \sin\theta & \cos\theta & 0 & 0 \end{bmatrix} \tag{20}$$

So the fifth and seventh harmonic currents after the transformation in x_1-y_1 coordinate axis are given by

$$\begin{bmatrix} I^6_{x1} \\ I^6_{y1} \end{bmatrix} = \begin{bmatrix} I_{xs}\sin(6w_et) + I_{xc}\cos(6w_et) \\ I_{ys}\sin(6w_et) + I_{yc}\cos(6w_et) \end{bmatrix} \tag{21}$$

where x_1-y_1 coordinate axis being the anti-synchronous reference frame which rotates at -w_e.

B. RESONANT CONTROLLER IN X-Y SUBSPACE

Resonant controller allows good performances of tracking of sinusoidal references of arbitrary frequency, which can achieve zero steady state error and is a substitute for the Proportional-Integral (PI) controllers carried out in positive and negative synchronous reference frames (SRF) to suppress the harmonic currents at the same time. It also has the merits on reducing the calculation complexity because it lacks in multiple coordinate transformations when it is compared with the traditional PI controllers carried out in several SRFs [14]. Besides, it can avoid the independence on motor parameters [11]–[18]. Therefore, it is a perfect option for the current controller in x-y subspace.

The resonant controller that provides perfect tracking of the harmonics of order h can be given as follows.

$$G^C_R(s) = K_R\frac{s\cos\phi - hw_e\sin\phi}{s^2 + (hw_e)^2} \tag{22}$$

where h being the harmonic order, the gain for the resonant controller can be represented by K_R, φ is an extra degree of freedom which gives a compensation angle at hw_e. So it can provide compensation for the phase delay induced by the computational as well as PWM update delay and inductive load [12], [13], [28] at hw_e in order to avoid the instability of the controller designed in x-y subspace. The Bode plot of the resonant controller (taking the resonant frequency 100rad/s for example) is depicted in Fig. 5.

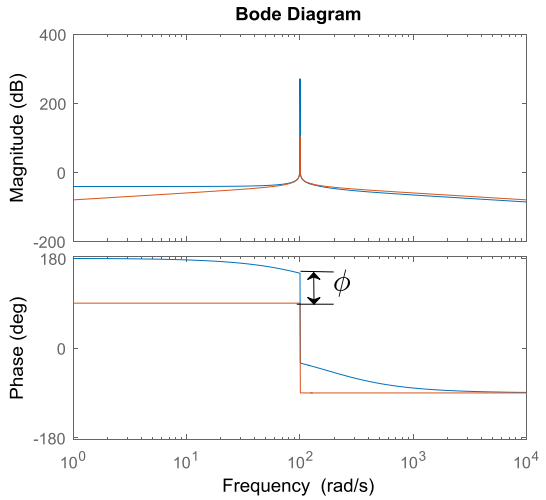

FIGURE 5. Bode diagram for the resonant controller.

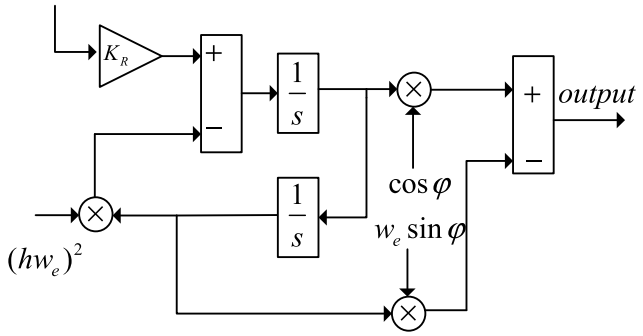

FIGURE 6. Block diagram of continuous resonant controller implemented by two integrators.

As discussed in [12], [13], resonant controller can be implemented with two integrators as illustrated in Fig. 6. hw_e is regulated online by means of the fundamental frequency to be controlled, which can be calculated by the phase locked loop (PLL) algorithm [29]. The method is employed widely because it offers the merits of frequency adaption and the integrators can be discretised separately.

As discussed before, two integrators should be discretised in order to make the resonant controller implemented in digital signal processor (DSP), since the expression is in the continuous domain and cannot be implemented directly in DSP. The good performance of tracking needs to place the poles at $e^{jw_eT_s}$ and $e^{-jw_eT_s}$ accurately. The denominator of the equation (22) after the product of both terms can be obtained as follows.

$$1 - 2z^{-1}\cos(hw_eT_s) + z^{-2} \tag{23}$$

In the process of discretization, the direct integrator adopts the forward Euler method, while the feedback integrator adopts the back Euler method is adopted, which can be shown in Fig. 7.

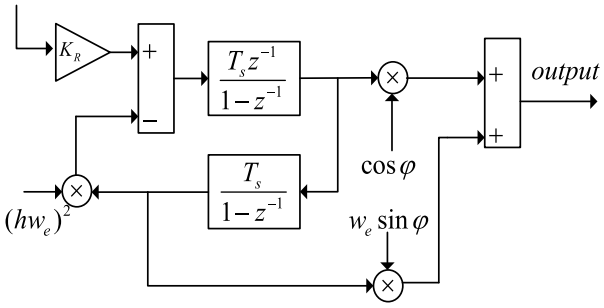

FIGURE 7. Digital resonant controller implemented with two integrators.

The denominator after the discretization depicted in Fig. 7 is

$$1 - 2z^{-1}(1 - h^2w_e^2T_S^2/2) + z^{-2} \tag{24}$$

One can see that the actual resonant frequency is not placed at the desired resonant frequency exactly when equation (23) is compared with equation (24).

Calculating the trigonometric function online will cost large amounts of resources. A substitute for this is Taylor series, which can make approximations of trigonometric function. And coshw_eT_s is approximated as in equation (25).

$$\cos hw_eT_s = \underbrace{1 - \frac{(hw_eT_s)^2}{2!} + \frac{(hw_eT_s)^4}{4!} - \cdots + \frac{(-1)^n(hw_eT_s)^{2n}}{(2n)!}}_{k=2n} \tag{25}$$

Therefore, the Taylor series can be used as a substitute for trigonometric function for the implementation of resonant controller in z-domain as shown in Fig. 8.

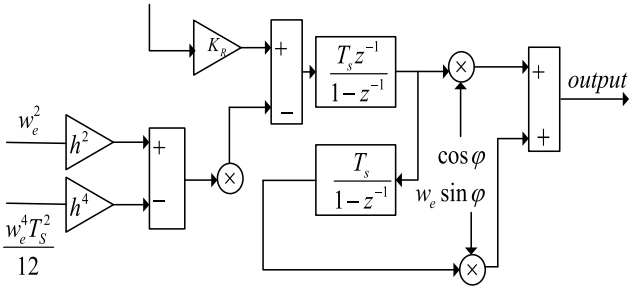

FIGURE 8. Block plot for digital resonant controller including the proposed resonant pole corrections.

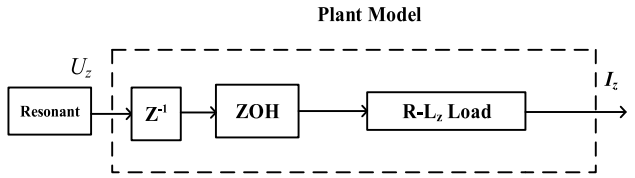

FIGURE 9. Current regulation system in *x-y* subspace.

C. STABILITY ANALYSIS IN X-Y SUBSPACE

Fig. 9 gives the current regulation system in *x-y* subspace which includes the plant model and resonant controller.

In order to avoid the instability of resonant controller in *x-y* subspace, φ should be accurately calculated. Here a ZOH equivalent model is established, where the effects of PWM can be reflected. Besides, it contains one sample control delay because of computational delay as well as PWM update delay. The plant model can be expressed as in equation (26).

$$\begin{aligned} P(z) = \frac{I_Z(z)}{U_Z(z)} &= z^{-1} * Z\left\{L\{Latch\}\frac{1}{L_z s + R}\right\} \\ &= z^{-1} * \left(1 - z^{-1}\right) * Z(\frac{1}{s(L_z s + R)}) \\ &= \frac{z^{-2}}{R}\frac{1 - e^{-RT_S/L_Z}}{1 - z^{-1}e^{-RT_S/L_Z}} \end{aligned} \tag{26}$$

where Z() being the Z transform, $z = e^{jw_e T_s}$.

It is noteworthy that L_Z and R represent the leakage inductance and resistance respectively, which differs from α-β subspace. For the purpose of making compensation for the phase delay, equation (27) is supposed to be fulfilled.

$$\phi = -\angle P(z) = -\arctan(\frac{e^{-RT_S/L_z}\sin(hw_e T_s) - \sin(2hw_e T_s)}{\cos(2hw_e T_s) - e^{-RT_S/L_z}\cos(hw_e T_s)}) \tag{27}$$

λ denotes the slope of equation (27) at the resonant frequency hw_e.

$$\begin{aligned} \lambda &= -\frac{\partial \angle P(z)}{\partial(hw_e)} \\ &= T_s\frac{2 + e^{-2RT_s/L_z} - 3e^{-RT_s/L_z}\cos(hw_e T_s)}{1 + e^{-2RT_s/L_z} - 2e^{-RT_s/L_z}\cos(hw_e T_s)} \end{aligned} \tag{28}$$

Because T_s is 0.00005s in this research, equation (29) is derived as follows.

$$\begin{aligned} e^{-2RT_s/L_z} &\approx 1 - \frac{2RT_s}{L_z} \approx 1 \\ e^{-RT_s/L_z} &\approx 1 - \frac{RT_s}{L_z} \approx 1 \end{aligned} \tag{29}$$

λ can be calculated based on the equations (28) and (29), which is about 3/2.

φ is 0 at the origin when w_e takes the value of 0. Therefore, the angle φ to be compensated can be approximately linearized in equation (30).

$$\phi = 1.5hw_e T_s \tag{30}$$

Therefore, U_x and U_y can be determined in the sinusoidal current modulation area, which is four-dimension current control. While U_x and U_y are 0 in sinusoidal voltage modulation area, which is two-dimension current control.

IV. CONTROL OF ADT_PMSM IN OVERMODULATION REGION

Six basic voltage vectors of the three-phase voltage source inverter (VSI) can form a regular hexagon as depicted in Fig. 4. Three basic voltage vectors $\overrightarrow{U_{sin}}$, $\overrightarrow{U_{hex}}$ and $\overrightarrow{U_{six}}$ are defined in this paper. $\overrightarrow{U_{sin}}$ defines the voltage vector corresponding to the maximal linear modulation index and the trajectory is the inscribed circle of the regular hexagon. The trace of $\overrightarrow{U_{hex}}$ is on the regular hexagon and the trace of $\overrightarrow{U_{six}}$ is on the vertex of the regular hexagon. The expressions of $\overrightarrow{U_{sin}}$, $\overrightarrow{U_{hex}}$ and $\overrightarrow{U_{six}}$ are given by

$$\overrightarrow{U_{\sin}} = \frac{U_{dc}}{\sqrt{3}}e^{j\theta} \tag{31}$$

$$\overrightarrow{U_{hex}} = \frac{U_{dc}}{\sqrt{3}\cos(\theta - \frac{(2n-1)\pi}{6})}e^{j\theta},\ \frac{(n-1)\pi}{3} \le \theta \le \frac{n\pi}{3} \tag{32}$$

$$\overrightarrow{U_{six}} = \frac{2U_{dc}}{3}e^{j\frac{(n-1)\pi}{3}},\ \frac{n\pi}{3} - \frac{\pi}{2} \le \theta \le \frac{n\pi}{3} - \frac{\pi}{6} \tag{33}$$

$$n = \left[\theta/60^0\right] + 1 \tag{34}$$

where θ represents the angle between the voltage vector $\overrightarrow{U_{\alpha\beta}}$ and switching vector (100) of phase windings ABC, and $\left[\theta/60^0\right]$ takes the largest integral value smaller than $\theta/60^0$. $\overrightarrow{U_{sin}}$ and $\overrightarrow{U_{hex}}$ share the same phase angle with $\overrightarrow{U_{\alpha\beta}}$, and $\overrightarrow{U_{six}}$ is the closet voltage vector to $\overrightarrow{U_{\alpha\beta}}$. The fundamental amplitude of $\overrightarrow{U_{sin}}$, $\overrightarrow{U_{hex}}$ and $\overrightarrow{U_{six}}$ are $0.577U_{dc}$, $0.606U_{dc}$ and $0.637U_{dc}$ respectively, corresponding to the modulation index (M) 0.9096, 0.9514 and 1.

A. OVERMODULATION REGION 1 (0.9069<M≤0.9514)

The modulation section is divided into 12 sectors as depicted in Fig. 4. Overmodulation region 1 is defined as follows. When the reference voltage vector exceeds the inscribed circle corresponding to $\overrightarrow{U_{sin}}$ of the hexagon and is within the circular trajectory of $\overrightarrow{U_{hex}}$. In this case, the part of reference voltage exceeding hexagon cannot be synthesized by the switching vectors. So the amplitude or the phase angle of reference voltage vector $\overrightarrow{U_{\alpha ß}}$ should be modified in order to make the average voltage of output equal to the reference voltage vector $\overrightarrow{U_{\alpha ß}}$ in a switching period.

Take sector 1 for example and other sectors can be derived in a similar way. According to the superposition principle, a linear combination of $\overrightarrow{U_{sin}}$ and $\overrightarrow{U_{hex}}$ will be used to reconstruct reference voltage vector $\overrightarrow{U_{\alpha ß}}$ as depicted in Fig.10.

The principle is that the phase of $\overrightarrow{U_{sin}}$ and $\overrightarrow{U_{hex}}$ is consistent with the reference voltage vector $\overrightarrow{U_{\alpha ß}}$. The weight coefficient of k_1 can make the fundamental amplitude of the synthesized

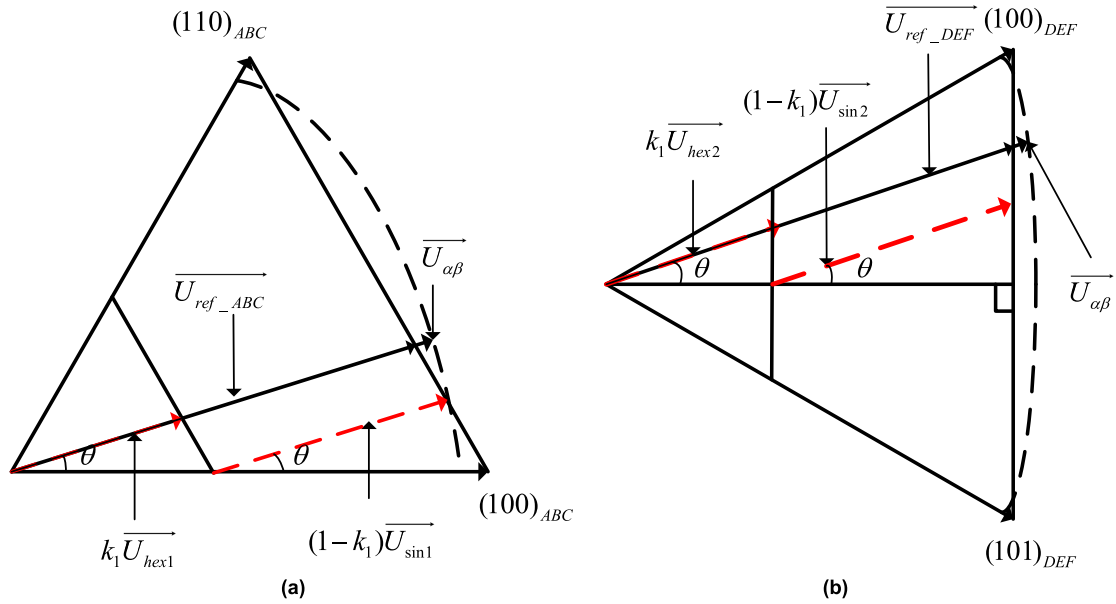

FIGURE 10. Overmodulation region 1. (a) Phase windings ABC. (b) Phase windings DEF.

vector equal to that of the reference voltage vector $\overrightarrow{U_{\alpha ß}}$, which can be expressed in equation (35).

$$k_1 = \frac{M - M_1}{M_2 - M_1} \tag{35}$$

The synthesized voltage vectors can be expressed as follows.

$$\begin{cases} \overrightarrow{U_{ref\_ABC}} = k_1 \overrightarrow{U_{hex1}} + (1 - k_1)\, \overrightarrow{U_{\sin 1}} \\ \overrightarrow{U_{ref\_DEF}} = k_1 \overrightarrow{U_{hex2}} + (1 - k_1)\, \overrightarrow{U_{\sin 2}} \end{cases} \tag{36}$$

where $M_1 = 0.9069$; $M_2 = 0.9514$, and M can be calculated based on equation (9). According to the VSD theory, U_α, $U_ß$, U_x and U_y in overmodulation region 1 can be given by

$$\begin{cases} U_\alpha = \left|\overrightarrow{U_{ref\_ABC}}\right| \cos\theta + \left|\overrightarrow{U_{ref\_DEF}}\right| \cos\theta \\ U_\beta = \left|\overrightarrow{U_{ref\_ABC}}\right| \sin\theta + \left|\overrightarrow{U_{ref\_DEF}}\right| \sin\theta \\ U_x = \left|\overrightarrow{U_{ref\_ABC}}\right| \cos\theta - \left|\overrightarrow{U_{ref\_DEF}}\right| \cos\theta \\ U_y = -\left|\overrightarrow{U_{ref\_ABC}}\right| \sin\theta + \left|\overrightarrow{U_{ref\_DEF}}\right| \sin\theta \end{cases} \tag{37}$$

In terms of equations (7), (8) and (36), the dwell time of each switching vector can be calculated.

In sector 1, in terms of equation (36), the amplitudes of the synthesized voltage vectors of the two three-phase windings in the fundamental subspace can be expressed as follows.

$$\begin{cases} \left|\overrightarrow{U_{ref\_ABC}}\right| = k_1 \dfrac{U_{dc}}{\sqrt{3}\sin(120^0 - \theta)} + (1 - k_1)\dfrac{U_{dc}}{\sqrt{3}} \\ \left|\overrightarrow{U_{ref\_DEF}}\right| = k_1 \dfrac{U_{dc}}{\sqrt{3}\cos\theta} + (1 - k_1)\dfrac{U_{dc}}{\sqrt{3}} \end{cases} \tag{38}$$

The fundamental amplitude can be analysed by Fourier Transform.

$$\begin{cases} f_1(\overrightarrow{U_{ref\_ABC}}) = f_1(\overrightarrow{U_{ref\_DEF}}) = \left|U_\alpha + jU_\beta\right| \\ f_1(\overrightarrow{U_{ref}}) = \int_0^{2\pi} \left|\overrightarrow{U_{ref}}\right| \cos\theta d\theta \end{cases} \tag{39}$$

where $f_1(U_{ref})$ is the fundamental component after the Fourier Transform. The fundamental amplitude of the synthesized voltage vector is equal to that of the reference voltage vector $\overrightarrow{U_{\alpha ß}}$ in the overmodulation region 1.

B. OVERMODULATION REGION 2 (0.9514<M≤1)

If reference voltage vector $\overrightarrow{U_{\alpha ß}}$ exceeds the circular trajectory corresponding to $\overrightarrow{U_{hex}}$, ADT_PMSM operates in overmodulation region 2. For the purpose of increasing the voltage output, a linear combination of $\overrightarrow{U_{hex}}$ and $\overrightarrow{U_{six}}$ is adopted to reconstruct the reference voltage vector $\overrightarrow{U_{\alpha ß}}$ as depicted in Fig.11 and also take sector 1 for example.

The phase angle of $\overrightarrow{U_{hex}}$ is still the same as that of the reference voltage vector $\overrightarrow{U_{\alpha ß}}$. $\overrightarrow{U_{six}}$ adopts the principle of proximity, which takes the nearest voltage vector to reference voltage vector $\overrightarrow{U_{\alpha ß}}$. The adjusted voltage vector is

$$\begin{cases} \overrightarrow{U_{ref\_ABC}} = k_2 \overrightarrow{U_{six1}} + (1 - k_2)\, \overrightarrow{U_{hex1}} \\ \overrightarrow{U_{ref\_DEF}} = k_2 \overrightarrow{U_{six2}} + (1 - k_2)\, \overrightarrow{U_{hex2}} \end{cases} \tag{40}$$

where $k_2 = \frac{M - M_2}{1 - M_2}$

The phase of the adjusted voltage vector is different from the original reference voltage vector $\overrightarrow{U_{\alpha ß}}$ after introducing the voltage vector $\overrightarrow{U_{six}}$. But it increases the voltage output capability.

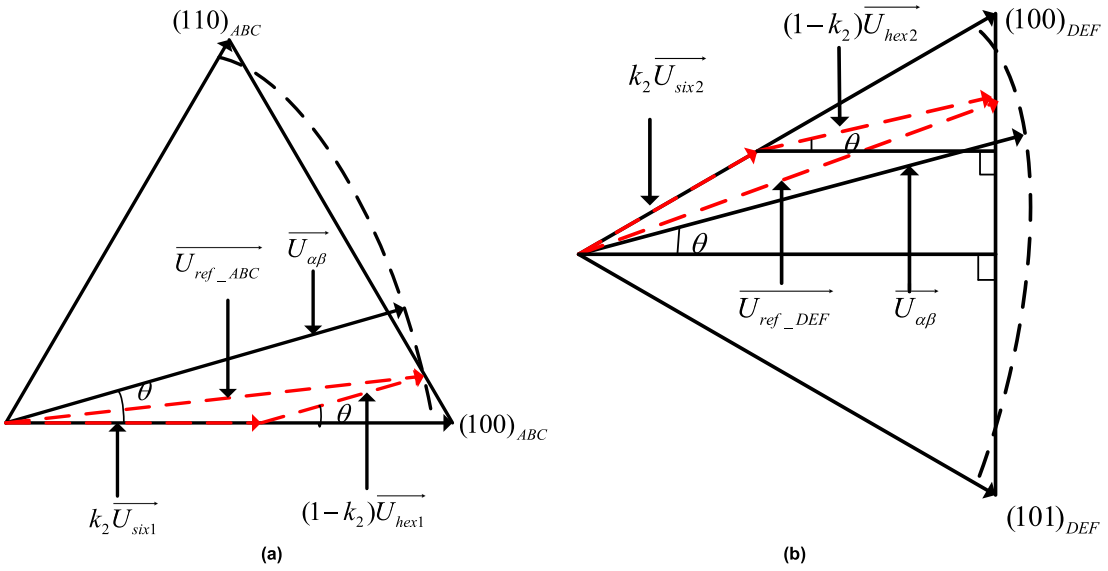

FIGURE 11. Overmodulation region 2. (a) Phase windings ABC. (b) Phase windings DEF.

According to the VSD theory [5], U_α, $U_ß$, U_x and U_y in overmodulation region 2 can be expressed as follows.

$$\begin{cases} U_\alpha = k_2\left|\overrightarrow{U_{six1}}\right| + (1-k_2)\left|\overrightarrow{U_{hex1}}\right|\cos\theta \\ \quad +k_2\left|\overrightarrow{U_{six2}}\right|\cos 30^0 + (1-k_2)\left|\overrightarrow{U_{hex2}}\right|\cos\theta \\ U_\beta = (1-k_2)\left|\overrightarrow{U_{hex1}}\right|\sin\theta \\ \quad +k_2\left|\overrightarrow{U_{six2}}\right|\sin 30^0 + (1-k_2)\left|\overrightarrow{U_{hex2}}\right|\sin\theta \\ U_x = k_2\left|\overrightarrow{U_{six1}}\right| + (1-k_2)\left|\overrightarrow{U_{hex1}}\right|\cos\theta \\ \quad -k_2\left|\overrightarrow{U_{six2}}\right|\cos 30^0 - (1-k_2)\left|\overrightarrow{U_{hex2}}\right|\cos\theta \\ U_y = -(1-k_2)\left|\overrightarrow{U_{hex1}}\right|\sin\theta \\ \quad +k_2\left|\overrightarrow{U_{six2}}\right|\sin 30^0 + (1-k_2)\left|\overrightarrow{U_{hex2}}\right|\sin\theta \end{cases} \tag{41}$$

According to equations (7), (8) and (41), the on-durations of switching vectors can be obtained.

In terms of equation (40) and Fig.11, the amplitudes of the synthesized voltage vectors of the two three-phase windings in the fundamental subspace can be expressed as follows.

$$\begin{cases} \overrightarrow{U_{ref\_ABC}} = U_{ref\_ABC\_\alpha} + jU_{ref\_ABC\_\beta} \\ \overrightarrow{U_{ref\_DEF}} = U_{ref\_DEF\_\alpha} + jU_{ref\_DEF\_\beta} \end{cases} \tag{42}$$

$U_{ref\_ABC\_\alpha}$, $U_{ref\_ABC\_ß}$, $U_{ref\_DEF\_\alpha}$ and $U_{ref\_DEF\_ß}$ can be expressed in equation (43).

$$\begin{cases} U_{ref\_ABC\_\alpha} = \dfrac{2U_{dc}}{3}k_2 + \dfrac{U_{dc}\cos\theta}{\sqrt{3}\sin(120^0-\theta)}(1-k_2) \\ U_{ref\_ABC\_\beta} = \dfrac{U_{dc}\sin\theta}{\sqrt{3}\sin(120^0-\theta)}(1-k_2) \\ U_{ref\_DEF\_\alpha} = \dfrac{U_{dc}}{\sqrt{3}} \\ U_{ref\_DEF\_\beta} = \dfrac{U_{dc}}{3}k_2 + \dfrac{U_{dc}}{\sqrt{3}}(1-k_2)\tan\theta \end{cases} \tag{43}$$

According to Fourier Transform, it can also be proved that the fundamental amplitude of the synthesized voltage vector is equal to that of the reference voltage vector $\overrightarrow{U_{ref}}$ in the overmodulation region 2.

From the above analysis, the proposed method which calculates the injected voltages in harmonic subspace in

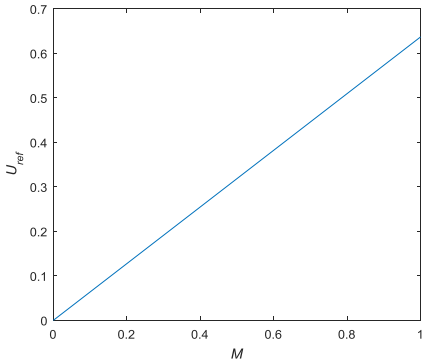

FIGURE 12. Fundamental amplitude of synthesized voltage vector as a function of *M*.

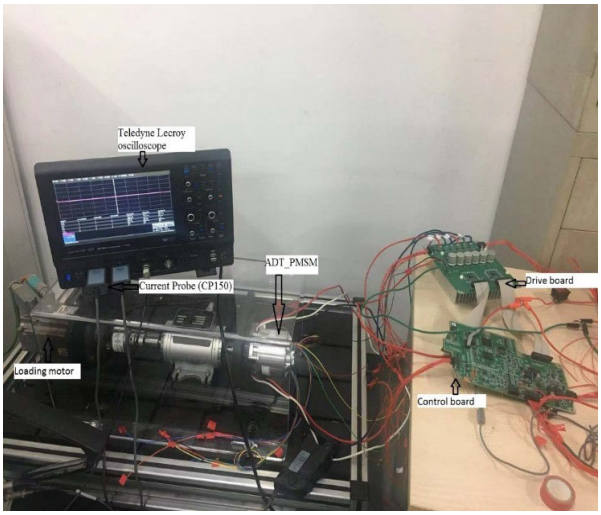

FIGURE 13. Experimental set-up.

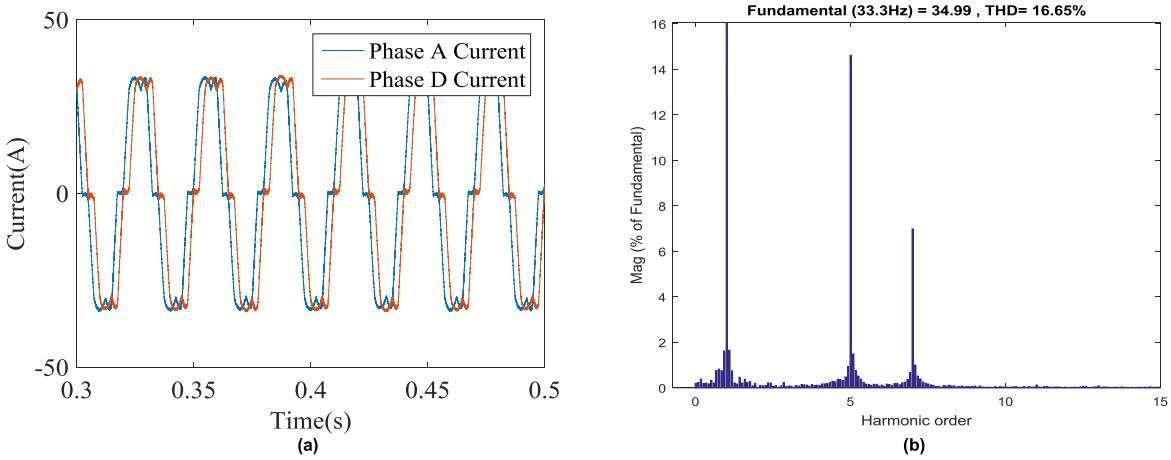

FIGURE 14. Performances with the suggested resonant controller not employed. (a) Phase A and Phase D currents. (b) THD of Phase A current.

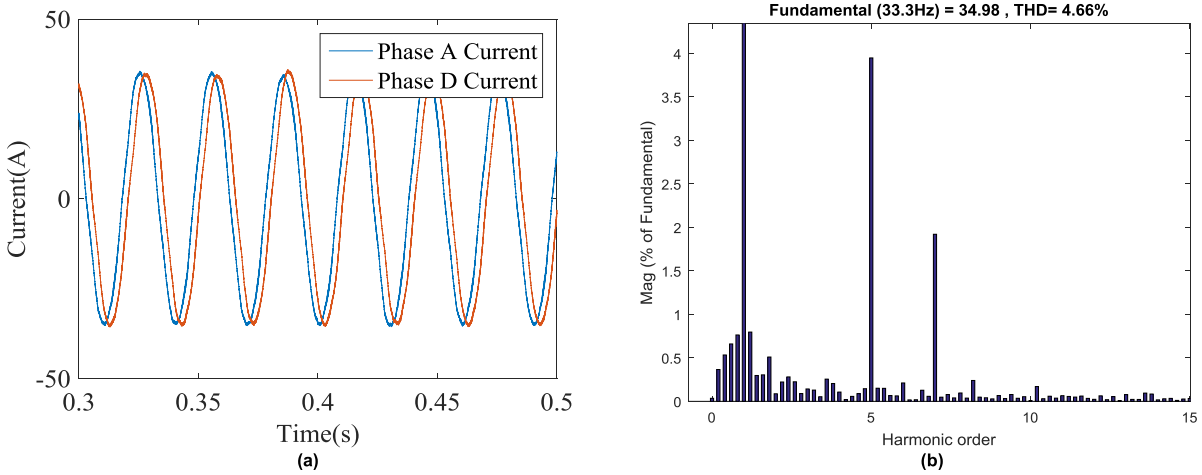

FIGURE 15. Performances after adopting resonant controller in harmonic subspace. (a) Phase A and Phase D currents. (b) THD of Phase A current.

TABLE 3. Machine parameters.

Parameter	Value
d-axis inductance	0.2mH
q-axis inductance	0.2mH
Leakage inductance	0.012mH
Permanent Magnet Flux	0.005Wb
Pole Pairs	5
Stator Resistance	0.0113Ω
Rated Torque	3.8±2.5%N*m
Rated speed	1260r/min
Rated Phase Current	50A
Rated Power	500W

TABLE 4. Computational time in different modulation regions.

Modulation Region	Computational time
Sinusoidal current modulation region	34.6μs
Sinusoidal voltage modulation region	29.7μs
Overmodulation region	35.2μs

overmodulation region is independent of machine parameters. Fig. 12 gives the relationship between fundamental amplitude of the synthesized voltage vector and modulation index. The value of longitudinal axis is normalized by the bus voltage U_{dc}. From the above analysis, the fundamental amplitude of synthesized voltage vector has a linear relationship with modulation index in the full modulation range, which can realize smooth transitions between different modulation regions.

TABLE 5. Performances of resonant controller with different orders.

Speed	k=2	k=4	k=6	k=8
200r/min	6.04%	5.52%	5.41%	5.38%
400r/min	5.32%	4.66%	4.71%	4.69%
600r/min	5.03%	4.41%	4.42%	4.42%
800r/min	4.52%	4.22%	4.21%	4.20%

V. EXPERIMENTAL VERIFICATION

For the purpose of verifying the effectiveness of the suggested strategy, experiments are carried out. The experimental platform shown in Fig. 13 is composed of an ADT_PMSM and two traditional two-level three-phase VSIs manufactured

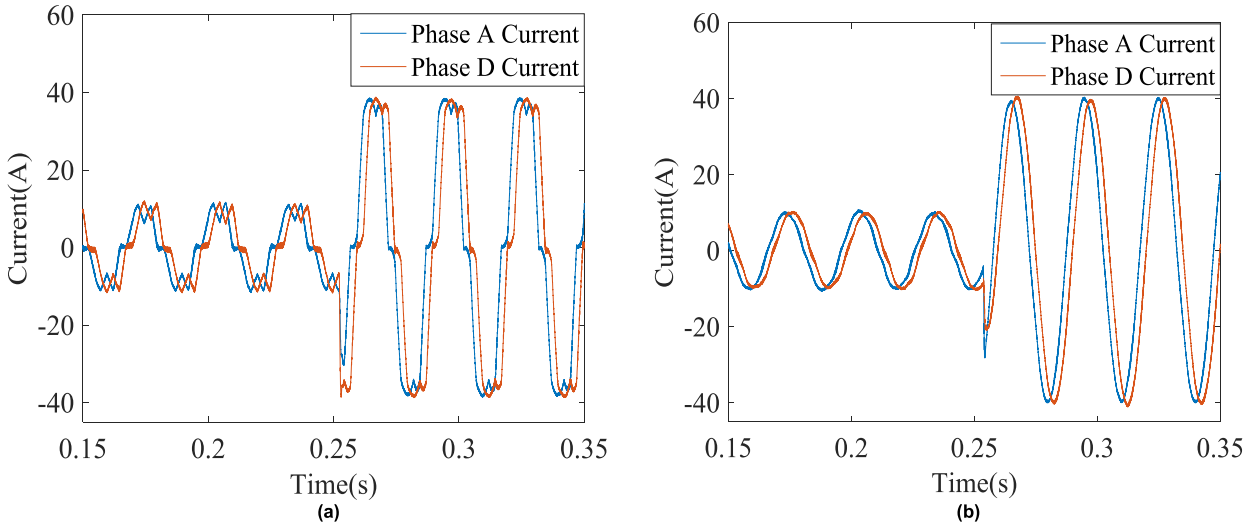

FIGURE 16. Performances under load transient state. (a) Without the suggested resonant controller in harmonic subspace. (b) With the suggested resonant controller in harmonic subspace.

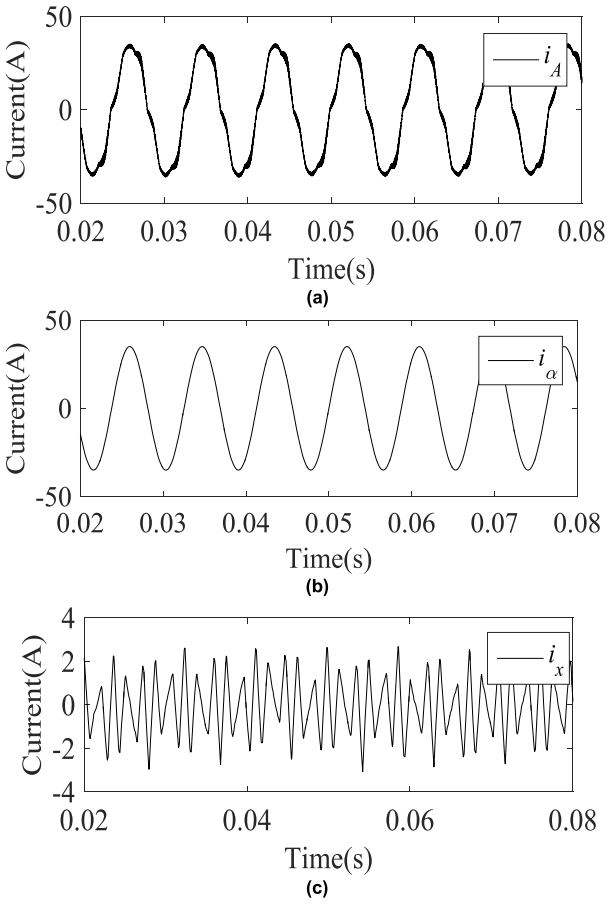

FIGURE 17. The waveforms of currents in sinusoidal voltage modulation region. (a) Phase current. (b) Current in α-β subspace. (c) Current in x-y subspace.

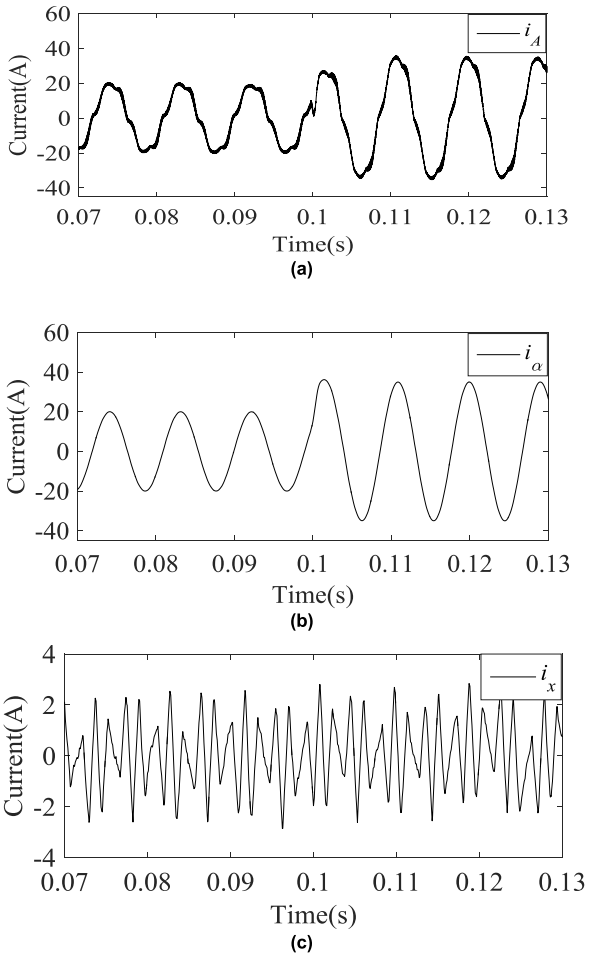

FIGURE 18. The waveforms of currents in sinusoidal voltage modulation region under load transient condition. (a) Phase current. (b) Current in α-β subspace. (c) Current in x-y subspace.

by Infineon. They are supplied by a direct current (DC) power and switching actions are performed under the control of a DSP (Infineon TC 277), where the proposed strategy is implemented. The switching frequency is 20kHz with $1\mu s$ set for the dead time. The phase currents are obtained by six hall-effect sensors and the sensor information for the speed is collected by a digital encoder. A BLDC motor gives the

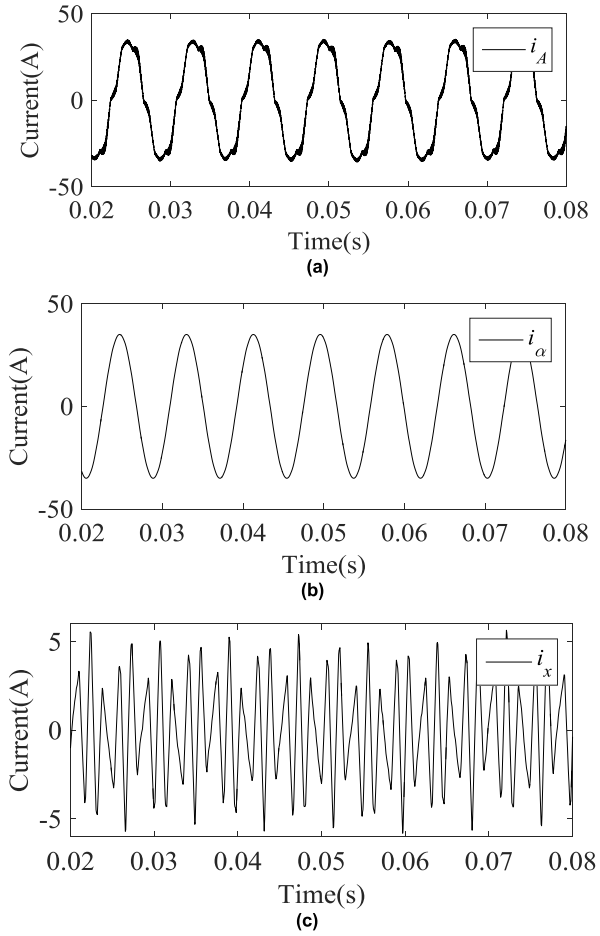

FIGURE 19. The waveforms of currents in overmodulation region 1. (a) Phase current. (b) Current in α-β subspace. (c) Current in x-y subspace.

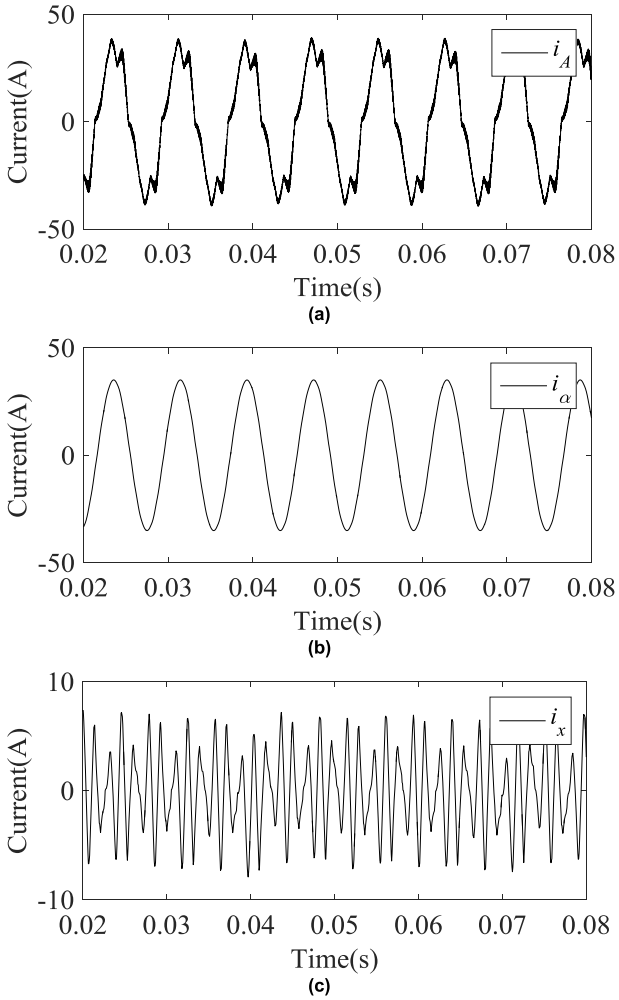

FIGURE 20. The waveforms of currents in overmodulation region 2. (a) Phase current. (b) Current in α-β subspace. (c) Current in x-y subspace.

load to the ADT_PMSM. And the load torque is dependent upon the speed. The phase currents are obtained by Current probe (CP150) and displayed by the Teledyne Lecroy oscilloscope (WaveSurfer 3024). The parameters of ADT_PMSM are given in Table 3.

The computational time of ADT_PMSM operating in three modulation regions is illustrated in Table 4. It is obvious that the computational load is acceptable.

A. ADT-PMSM OPERATING IN SINUSOIDAL CURRENT MODULATION AREA

Fig. 14 illustrates the experimental results in the sinusoidal current modulation area where resonant controller is not adopted. And the phase current is 35A.

The ADT-PMSM operates under current control mode and the mechanical speed is maintained at 400r/min by dynamometer. U_x and U_y are set to be 0. It can be found that the phase currents are severely distorted because of the nonlinear characteristics of VSI. And the total harmonic distortion (THD) is 16.65%. Besides, it is obvious that the 5th and 7th harmonic currents make up the majority part of harmonic currents

Fig. 15 shows the experimental results in the sinusoidal current modulation area where the proposed resonant controller is adopted. For the purpose of obtaining an appropriate k value, the experimental results of different orders for the pole correction are given in Table 5 where the phase current takes the value of 35A. One can find that the implementation of pole correction can utilize the fourth-order approximation ($k = 4$), since an even bigger value for k can make little contributions to the reduction of harmonic currents, but this will increase the computational complexity.

Considerable reduction of harmonic currents can be found as illustrated in Fig. 15. The phase currents have been improved a lot after employing the proposed resonant controller ($k = 4$) and the THD of phase A current value is reduced to 4.66% as shown in Fig 15(b) through the proposed resonant controller.

For the purpose of testing the performances under transient state, load step change is applied to ADT_PMSM and corresponding experiments are carried out. Fig. 16 gives the experimental results when the ADT_PMSM undergoes a load step change. The phase current undergoes a change from 10 A to 40A and mechanical speed is still kept at 400r/min. One can see that the phase currents have obtained significant

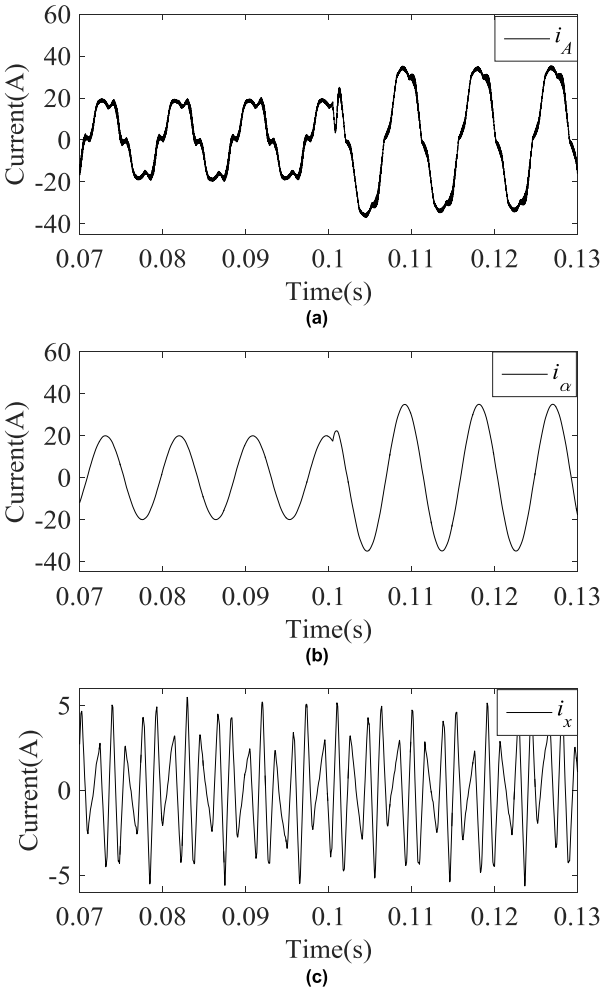

FIGURE 21. The waveforms of currents in overmodulation region 1 under load transient condition. (a) Phase current. (b) Current in α-β subspace. (c) Current in x-y subspace.

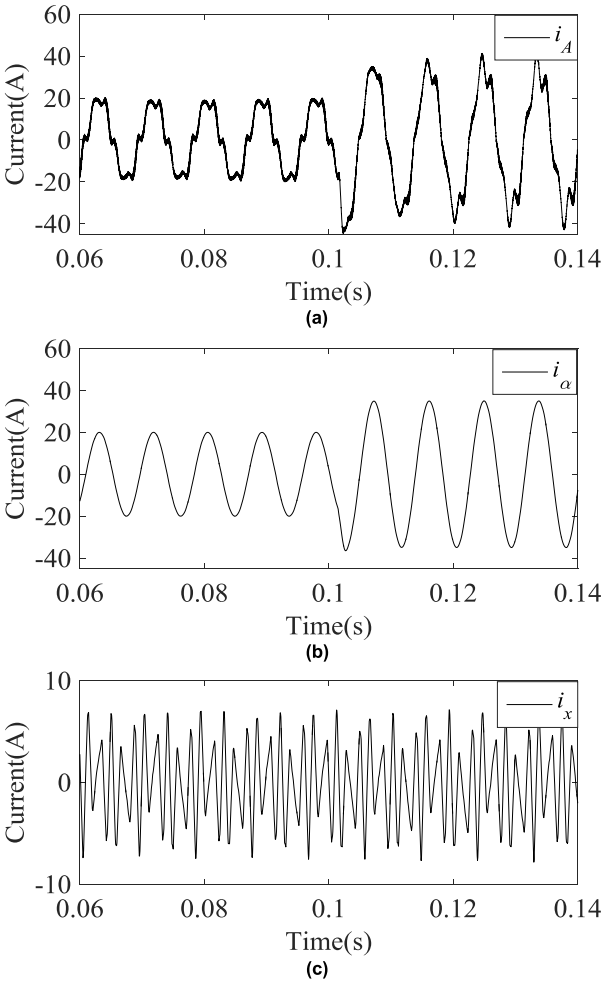

FIGURE 22. The waveforms of currents in overmodulation region 2 under load transient condition. (a) Phase current. (b) Current in α-β subspace. (c) Current in x-y subspace.

improvements after employing the proposed resonant controller. Therefore, a conclusion can be made that the proposed scheme can offer continuous and steady compensation with no abrupt break under transient state.

B. ADT-PMSM OPERATING IN SINUSOIDAL VOLTAGE MODULATION AREA

Fig. 17 shows the experimental performances when ADT_PMSM operates in the sinusoidal voltage modulation area under the current control loop. Fig.17 (a) shows the phase A current, i_α is the current in α-β subspace and i_x is the current in x-y subspace which are depicted in Fig.17 (b) and Fig.17 (c) respectively.

According to the VSD theory [18], i_A is equal to the sum of i_α and i_x. In practice, i_α and i_x cannot be displayed by the oscilloscope, so the phase currents are stored in order to calculate i_α and i_x based on the VSD matrix. From Fig. 17, one can see that current harmonics will appear in x-y subspace owing to the dead time effects in sinusoidal voltage modulation area. Nearly no current distortions exist in α-β subspace, which will not affect the torque output performance.

In order to verify the transient performances, Fig. 18 gives the experimental results when a load step change is applied to ADT_PMSM in the sinusoidal voltage modulation region. The phase current suffers from 20A to 35A. It is apparent that nearly no current distortions exist in the α-β subspace under load transient state. So the output torque performance will not be influenced even if the load changes.

C. ADT-PMSM OPERATING IN OVERMODULATION AREA

Fig. 19 and Fig. 20 show the current waveforms in the overmodulation region 1 and overmodulation region 2 respectively. Compared to the sinusoidal voltage modulation area, more harmonic currents exist in x-y subspace due to the extra voltage harmonics which are injected into x-y subspace. Besides, the distortions of phase currents in overmodulation region 2 are more severe than those in overmodulation region 1, because more harmonic voltages are injected into x-y subspace in overmodulation region 2. It is obvious that nearly no current distortions exist in the α-β subspace in overmodulation regions. So the output torque performance will not be influenced.

In order to test the transient performances, Fig. 21 and Fig. 22 give the experimental performances under a load step change in the overmodulation region 1 and 2 respectively. The phase current suffers from 20A to 35A. Although a lot of current harmonics exist in the phase current, nearly no current distortions exist in the α-β subspace under load transient state, which means that the output torque performance will not be influenced even under load transient state in the overmodulation region.

VI. CONCLUSION

In this paper, the total modulation range of ADT_PMSM is divided into three modulation regions according to the dimensions of current control and voltage modulation range, which are sinusoidal current modulation region, sinusoidal voltage modulation region and overmodulation region. In sinusoidal current modulation region, resonant controller is adopted in x-y subspace to eliminate harmonic currents, which takes the pole correction into consideration. In sinusoidal voltage modulation region, the command voltage U_x and U_y are set to be zero in x-y subspace, which is two dimensional current control. The reference voltage vectors in x-y subspace when ADT_PMSM operates in the overmodulation regions are calculated based on the VSD theory and superposition principle. A novel SVPWM technique for ADT_PMSM is presented to achieve the smooth transition from linear modulation region to overmodulation region. And the fundamental amplitude of the synthesized voltage vector is proportional to the modulation index in the full modulation range. The experimental performances validate the feasibility of proposed control strategy in both steady and transient states.

REFERENCES

[1] Y. Geng, Z. Lai, Y. Li, D. Wang, R. Chen, and P. Zheng, "Sensorless fault-tolerant control strategy of six-phase induction machine based on harmonic suppression and sliding mode observer," *IEEE Access*, vol. 7, pp. 110086–110102, 2019.

[2] F. M. Zaihidee, S. Mekhilef, and M. Mubin, "Application of fractional order sliding mode control for speed control of permanent magnet synchronous motor," *IEEE Access*, vol. 7, pp. 101765–101774, 2019.

[3] Y. Demir and M. Aydin, "A novel dual three-phase permanent magnet synchronous motor with asymmetric stator winding," *IEEE Trans. Magn.*, vol. 52, no. 7, pp. 1–5, Jul. 2016.

[4] S. Mekhilef, M. N. A. Kadir, and Z. Salam, "Digital control of three phase three-stage hybrid multilevel inverter," *IEEE Trans. Ind. Informat.*, vol. 9, no. 2, pp. 719–727, May 2013.

[5] S. Mekhilef and M. N. A. Kadir, "Novel vector control method for three-stage hybrid cascaded multilevel inverter," *IEEE Trans. Ind. Electron.*, vol. 58, no. 4, pp. 1339–1349, Apr. 2011.

[6] M. K. Menshawi, M. N. Abdul Kadir, and S. Mekhilef, "Voltage vector approximation control of multistage—Multilevel inverter using simplified logic implementation," *IEEE Trans. Ind. Informat.*, vol. 9, no. 4, pp. 2052–2062, Nov. 2013.

[7] G. Grandi, G. Serra, and A. Tani, "Space vector modulation of a six-phase VSI based on three-phase decomposition," in *Proc. Int. Symp. Power Electron., Electr. Drives, Autom. Motion*, Ischia, Italy, Jun. 2008, pp. 674–679.

[8] A. Taheri, "Harmonic reduction of direct torque control of six-phase induction motor," *ISA Trans.*, vol. 63, pp. 299–314, Jul. 2016.

[9] Y. Ren and Z. Q. Zhu, "Reduction of both harmonic current and torque ripple for dual three-phase permanent-magnet synchronous machine using modified switching-table-based direct torque control," *IEEE Trans. Ind. Electron.*, vol. 62, no. 11, pp. 6671–6683, Nov. 2015.

[10] K. D. Hoang, M. Foster, Z.-Q. Zhu, and Y. Ren, "Modified switching-table strategy for reduction of current harmonics in direct torque controlled dual-three-phase permanent magnet synchronous machine drives," *IET Electr. Power Appl.*, vol. 9, no. 1, pp. 10–19, Jan. 2015.

[11] H.-M. Ryu, J.-W. Kim, and S.-K. Sul, "Synchronous frame current control of multi-phase synchronous motor. Part I. Modeling and current control based on multiple d-q spaces concept under balanced condition," in *Proc. Conf. Rec. IEEE Ind. Appl. Conf., 39th IAS Annu. Meeting.*, Seattle, WA, USA, Oct. 2004, p. 63.

[12] A. G. Yepes, F. D. Freijedo, J. Doval-Gandoy, Ó. López, J. Malvar, and P. Fernandez-Comesaña, "Effects of discretization methods on the performance of resonant controllers," *IEEE Trans. Power Electron.*, vol. 25, no. 7, pp. 1692–1712, Jul. 2010.

[13] A. G. Yepes, F. D. Freijedo, Ó. Lopez, and J. Doval-Gandoy, "High-performance digital resonant controllers implemented with two integrators," *IEEE Trans. Power Electron.*, vol. 26, no. 2, pp. 563–576, Feb. 2011.

[14] A. G. Yepes, J. Malvar, A. Vidal, O. Lopez, and J. Doval-Gandoy, "Current harmonics compensation based on multiresonant control in synchronous frames for symmetrical n-phase machines," *IEEE Trans. Ind. Electron.*, vol. 62, no. 5, pp. 2708–2720, May 2015.

[15] A. G. Yepes, J. Doval-Gandoy, F. Baneira, D. Perez-Estevez, and O. Lopez, "Current harmonic compensation for n -phase machines with asymmetrical winding arrangement and different neutral configurations," *IEEE Trans. Ind. Appl.*, vol. 53, no. 6, pp. 5426–5439, Nov. 2017.

[16] Z. Ruan, W. Song, and Y. Yan, "Current harmonic suppression for dual three-phase permanent magnet synchronous motor drives," *IEEE Access*, vol. 7, pp. 143888–143898, Sep. 2019.

[17] L. Yuan, M.-L. Chen, J.-Q. Shen, and F. Xiao, "Current harmonics elimination control method for six-phase PM synchronous motor drives," *ISA Trans.*, vol. 59, pp. 443–449, Nov. 2015.

[18] H. S. Che, E. Levi, M. Jones, W.-P. Hew, and N. A. Rahim, "Current control methods for an asymmetrical six-phase induction motor drive," *IEEE Trans. Power Electron.*, vol. 29, no. 1, pp. 407–417, Jan. 2014.

[19] K. Gopakumar, V. T. Ranganathan, and S. R. Bhat, "An efficient PWM technique for split phase induction motor operation using dual voltage source inverters," in *Proc. Conf. Rec. IEEE Ind. Appl. Conf. 28th IAS Annu. Meeting*, Toronto, ON, Canada, vol. 1, Oct. 1993, pp. 582–587.

[20] G. Renukadevi and K. Rajambal, "FPGA implementation of SVPWM technique for asymmetrical six-phase VSI," in *Proc. Int. Conf. Emerg. Trends Electr. Eng. Energy Manage. (ICETEEEM)*, Chennai, India, Dec. 2012, pp. 333–338.

[21] D. Hadiouche, L. Baghli, and A. Rezzoug, "Space-vector PWM techniques for dual three-phase AC machine: Analysis, performance evaluation, and DSP implementation," *IEEE Trans. Ind. Appl.*, vol. 42, no. 4, pp. 1112–1122, Jul. 2006.

[22] K. Marouani, L. Baghli, D. Hadiouche, A. Kheloui, and A. Rezzoug, "A new PWM strategy based on a 24-sector vector space decomposition for a six-phase VSI-fed dual stator induction motor," *IEEE Trans. Ind. Electron.*, vol. 55, no. 5, pp. 1910–1920, May 2008.

[23] C. Zhou, G. Yang, and J. Su, "PWM strategy with minimum harmonic distortion for dual three-phase permanent-magnet synchronous motor drives operating in the overmodulation region," *IEEE Trans. Power Electron.*, vol. 31, no. 2, pp. 1367–1380, Feb. 2016.

[24] D. Yazdani, S. A. Khajehoddin, A. Bakhshai, and G. Joos, "Full utilization of the inverter in split-phase drives by means of a dual three-phase space vector classification algorithm," *IEEE Trans. Ind. Electron.*, vol. 56, no. 1, pp. 120–129, Jan. 2009.

[25] K. Zhou and D. Wang, "Relationship between space-vector modulation and three-phase carrier-based PWM: A comprehensive analysis [three-phase inverters]," *IEEE Trans. Ind. Electron.*, vol. 49, no. 1, pp. 186–196, Feb. 2002.

[26] G. Carrasco and C. A. Silva, "Space vector PWM method for five-phase two-level VSI with minimum harmonic injection in the overmodulation region," *IEEE Trans. Ind. Electron.*, vol. 60, no. 5, pp. 2042–2053, May 2013.

[27] M. J. Durán, J. Prieto, and F. Barrero, "Space vector PWM with reduced common-mode voltage for five-phase induction motor drives operating in overmodulation zone," *IEEE Trans. Power Electron.*, vol. 28, no. 8, pp. 4030–4040, Aug. 2013.

[28] H. Kim, M. W. Degner, J. M. Guerrero, F. Briz, and R. D. Lorenz, "Discrete-time current regulator design for AC machine drives," *IEEE Trans. Ind. Appl.*, vol. 46, no. 4, pp. 1425–1435, Jul. 2010.
[29] H. X. Nguyen, T. N.-C. Tran, J. W. Park, and J. W. Jeon, "An adaptive linear-neuron-based third-order PLL to improve the accuracy of absolute magnetic encoders," *IEEE Trans. Ind. Electron.*, vol. 66, no. 6, pp. 4639–4649, Jun. 2019.

YUAN ZHU was born in Jiangsu, China, in 1976. He received the double B.S. degree in automotive engineering and computer application technology and the Ph.D. degree in automotive engineering from Tsinghua University, China, in 1998 and 2003, respectively.

He has been an Assistant Research Scientist with the Department of Automotive Engineering, Tsinghua University, from 2003 to 2005. Since 2005, he has been working as an Associate Professor with the Sino-German School for Postgraduate Studies, Tongji University. Since 2014, he is responsible for the Hans L. Merkle Foundation-Bosch Endowed Chair for Automotive Systems at Tongji University. His current research interests include simulation and control for electric drive systems and embedded software systems.

WEISONG GU received the B.S. degree in vehicle engineering from the Wuhan University of Technology, Wuhan, Hubei, China, in 2014, and the M.S. degree in vehicle engineering from Tongji University, Shanghai, China, in 2017, where he is currently pursuing the Ph.D. degree in vehicle engineering.

His research interest includes the control of electric motors in vehicle.

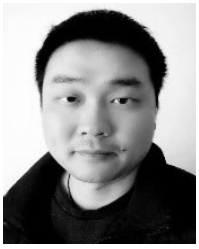

KE LU was born in Jiangsu, China in 1983. He received the B.S. degree in automation and the M.S. and Ph.D. degrees in computer science and vehicle engineering from Tongji University, Shanghai, China, in 2006, 2009, and 2018, respectively.

He is currently an Engineer with the School of Automotive Studies, Tongji University. His main research interests include motor control for electric vehicles, perception algorithm for autonomous vehicles, and functional safety.

ZHIHONG WU (Member, IEEE) was born in Zhejiang, China, in 1961. He received the B.S. and M.S. degrees in electrical engineering from Zhejiang University, China, and the Dr.-Ing. degree from Technical University Berlin, Germany.

He worked as a Research and Development Engineer with Danfoss Antriebs- und Regeltechnik GmbH, Germany. He is currently the Deputy Dean of the Sino-German College for Postgraduate Studies (CDHK), Tongji University, an Infineon Endowed Chair Professor for Embedded Systems, the Director of Infineon-Tongji Automotive Electronics Joint Laboratory, and the Director of the Tongji-Vector Automotive Technology Joint Laboratory. His main research interests include motor control for electric vehicles, embedded software systems, perception algorithm for autonomous vehicles, and functional safety.

Dr. Wu is a member of the Board of Director of Power Converter and Intelligent Motion (PCIM) Asia and the International Science Committee of European Power Electronics (EPE). He is the Vice Chairman of the Shanghai Power Supply Association.